Nanoscale Advances

ROYAL SOCIETY OF CHEMISTRY

PAPER

Cite this: Nanoscale Adv., 2022, 4, 1191

Modulation of electrical properties in $MoTe_2$ by XeF_2-mediated surface oxidation†

Eunji Ji,‡[a] Jong Hun Kim,‡[ade] Wanggon Lee,[b] June-Chul Shin,[d] Hyungtak Seo,[c] Kyuwook Ihm,[f] Jin-Woo Park[a] and Gwan-Hyoung Lee*[degh]

Transition metal dichalcogenides (TMDs) are promising candidates for the semiconductor industry owing to their superior electrical properties. Their surface oxidation is of interest because their electrical properties can be easily modulated by an oxidized layer on top of them. Here, we demonstrate the XeF_2-mediated surface oxidation of 2H-$MoTe_2$ (alpha phase $MoTe_2$). $MoTe_2$ exposed to XeF_2 gas forms a thin and uniform oxidized layer (~2.5 nm-thick MoO_x) on $MoTe_2$ regardless of the exposure time (within ~120 s) due to the passivation effect and simultaneous etching. We used the oxidized layer for contacts between the metal and $MoTe_2$, which help reduce the contact resistance by overcoming the Fermi level pinning effect by the direct metal deposition process. The $MoTe_2$ field-effect transistors (FETs) with a MoO_x interlayer exhibited two orders of magnitude higher field-effect hole mobility of 6.31 $cm^2 V^{-1} s^{-1}$ with a high on/off current ratio of ~10^5 than that of the $MoTe_2$ device with conventional metal contacts (0.07 $cm^2 V^{-1} s^{-1}$). Our work shows a straightforward and effective method for forming a thin oxide layer for $MoTe_2$ devices, applicable for 2D electronics.

Received 1st November 2021
Accepted 4th January 2022

DOI: 10.1039/d1na00783a

rsc.li/nanoscale-advances

Introduction

Transition metal dichalcogenide (TMD) semiconductors have been actively studied owing to their great potential in advanced electronics and unprecedented physical properties.[1–8] Electronic devices based on exfoliated TMDs have a thickness limit of a few atomic layers with dangling-bond-free passivated surfaces because individual layers of TMDs are held together with weak van der Waals forces. Among these TMDs, 2H-$MoTe_2$ (alpha phase $MoTe_2$) has a moderate indirect band gap (E_g) of 0.88 eV in bulk[9,10] and a direct band gap (E_g) of 1.1 eV in a monolayer form.[11] The moderate band gap of $MoTe_2$, similar to that of bulk silicon, makes it a promising candidate for various electronic applications, such as transistors, complementary logic devices, optoelectronic devices, and memory.[12,13] It is well known that the Schottky barrier height between $MoTe_2$ and the metal is very weakly dependent on the work function of the metal due to the strong Fermi level pinning effect, leading to a high contact resistance (R_c).[14] Although the Schottky barrier height is determined by the work function of the contact metal according to the Schottky–Mott rule, a strong Fermi level pinning effect and high contact resistance (R_c) are caused by physical bombardment during the metal deposition process, leading to crystallinity damage in $MoTe_2$.[15] It was recently found that transition metal oxides (TMOs) are suitable candidates as buffer layers between TMDs and metals.[16,17] The fabrication of TMOs has been reported using various methods, such as oxygen plasma treatment,[18] atomic layer deposition (ALD),[19] UV–ozone treatment[20] and thermal evaporation.[21] However, surface treatment methods can easily damage TMDs, leading to reduced crystallinity and increased surface roughness.[15,22] The atomic thickness of TMD flakes gives rise to these issues, degrading the electronic properties of the device.

In this work, we demonstrate the fabrication of a thin and uniform oxidized layer on top of $MoTe_2$ by exposing it to XeF_2 gas. The oxidized layer had a uniform thickness of ~2.5 nm regardless of the exposure time (within ~120 s) due to the passivation effect and simultaneous etching. The non-stoichiometric oxide layer has a high work function, allowing for p-doping of the underlying $MoTe_2$. The $MoTe_2$ device showed a high field-effect hole mobility of 6.31 $cm^2 V^{-1} s^{-1}$ with a high

[a]Department of Material Science and Engineering, Yonsei University, Seoul, 03722, Korea
[b]Department of Energy Systems Research, Ajou University, Suwon 16499, Republic of Korea
[c]Department of Materials Science and Engineering, Ajou University, Suwon 16499, Republic of Korea
[d]Department of Materials Science and Engineering, Seoul National University, Seoul 08826, Korea
[e]Research Institute of Advanced Materials (RIAM), Seoul National University, Seoul 08826, Korea
[f]Department of Physics and Pohang Accelerator Laboratory, Pohang University of Science and Technology, 37673, Pohang, Korea
[g]Institute of Engineering Research, Seoul National University, Seoul 08826, Korea
[h]Institute of Applied Physics, Seoul National University, Seoul 08826, Korea. E-mail: gwanlee@snu.ac.kr

† Electronic supplementary information (ESI) available. See DOI: 10.1039/d1na00783a

‡ These authors contributed equally: Eunji Ji and Jong Hun Kim.

This article is licensed under a Creative Commons Attribution-NonCommercial 3.0 Unported Licence.

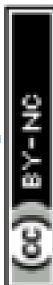

© 2022 The Author(s). Published by the Royal Society of Chemistry

on/off current ratio of ~10^5. The palladium (Pd) metal can easily tunnel to $MeTe_2$ layer by MoO_x layer. The mobility is two orders of magnitude higher than that of the $MoTe_2$ device with conventional metal contacts.

Results and discussions

The mechanically exfoliated $MoTe_2$ flakes were exposed to XeF_2 gas at 1.8 torr for different treatment times. The optical microscope images of the $MoTe_2$ flakes in Fig. 1a show the contrast change before and after XeF_2 exposure for 150 s. The corresponding surface morphology was also identified by using atomic force microscopy (AFM), as shown in Fig. 1b. As confirmed using AFM images, even after the treatment, the overall structure was not changed, exhibiting the relatively uniform surface morphologies; however, the optical contrast of the flakes was significantly suppressed after XeF_2 exposure. The depression in the optical contrast may be attributed to the change in the optical path caused by mediating the refractive properties of $MoTe_2$ with XeF_2 treatment.[23,24] Fig. 1c shows the height profiles created by following the dashed lines in Fig. 1b. The thickness of the fourth layer (4 L) and third layer (3 L) $MoTe_2$ was measured to be ~3.1 nm and ~2.4 nm before XeF_2 exposure (blue dashed lines in Fig. 1b), respectively. However, the thickness remained approximately the same even after XeF_2 exposure (red dashed lines in Fig. 1b), *i.e.*, ~3.0 nm and ~2.3 nm, respectively. Fig. 1d and e show the Raman spectra of the 3 L and 4 L regions (blue and red dots in Fig. 1a, respectively) of the $MoTe_2$ flakes. $MoTe_2$ showed the representative phonon modes of $A_g{}^1$ (~170 cm^{-1}), $E_{2g}{}^1$ (~234 cm^{-1}), and $B_{2g}{}^1$ (~289 cm^{-1}).[25] Meanwhile, monolayer (1 L) $MoTe_2$ was found to have a prominent peak of $E_{2g}{}^1$ and a weaker peak of A_{1g} at ~235 cm^{-1} and ~174 cm^{-1}, respectively.[26] The Raman spectra of 3 L $MoTe_2$ in Fig. 1d show that all Raman modes were depressed after XeF_2 exposure. However, only the $B_{2g}{}^1$ mode of 4 L $MoTe_2$ disappeared after XeF_2 exposure, maintaining other Raman peaks (Fig. 1e). This indicates that a few topmost layers of $MoTe_2$ were substituted with a different material with a comparable atomic thickness, while the subsurface remained as $MoTe_2$. It was expected that unidentified layers were produced upon XeF_2 exposure. In particular, the Raman mode related to MoO_3 [27] and MoO_2 [28,29] cannot be observed. Therefore, Raman spectroscopy failed to provide clear evidence of it.

ESI, Fig. S2a and b† show the optical microscope images and Raman spectra of 1 L and 2 L of $MoTe_2$ before and after XeF_2 exposure at 1.8 torr for 60 s, respectively. After XeF_2 treatment, the intensities of $E_{2g}{}^1$ and $B_{2g}{}^1$ in 2 L $MoTe_2$ were slightly lower

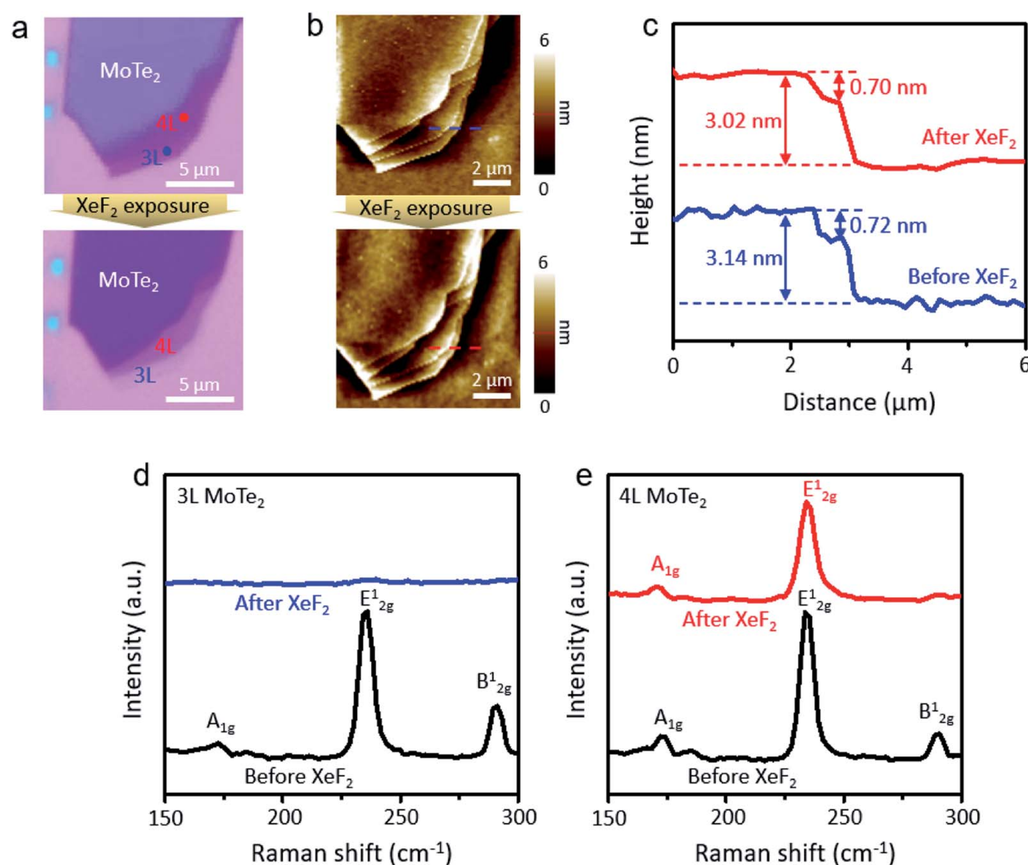

Fig. 1 (a) Optical microscope images of few layer $MoTe_2$ before and after XeF_2 exposure at 1.8 torr for 150 s, (b) AFM topology images of $MoTe_2$ before and after XeF_2 treatment, (c) height profile of $MoTe_2$ before (blue line) and after (red line) XeF_2 treatment, (d) the Raman spectra of 3 L $MoTe_2$ (blue dot region) in Fig. 1a before (black line) and after (red line) XeF_2 treatment, and (e) the Raman spectra of 4 L $MoTe_2$ (red dot region) in Fig. 1a before (black line) and after (red line) XeF_2 treatment.

 © 2022 The Author(s). Published by the Royal Society of Chemistry

than those before XeF_2 exposure. However, the B_{2g}^1 mode in 2 L disappeared after XeF_2 exposure in the Raman spectrum, indicating that 2 L transforms into 1 L at 1.8 torr for 60 s (the graph at the top in the red-colored region in ESI, Fig. S2b†). All modes in 1 L of $MoTe_2$ disappeared after XeF_2 exposure, indicating that its crystal structure vanished (the graphs in the blue-colored region of ESI, Fig. S2b†). The E_{2g}^1 mode of XeF_2-exposed 2 L was downshifted by 2.18 cm^{-1} compared to that of pristine 1 L of $MoTe_2$ (before XeF_2 exposure). The A_g^1 mode showed an upshift from 171.94 cm^{-1} (pristine 1 L of $MoTe_2$) to 172.15 cm^{-1} (XeF_2-exposed 2 L of $MoTe_2$), which is another evidence for p-type doping of $MoTe_2$ after XeF_2 treatment.[30] We used the Raman mapping method to verify the uniform treatment of XeF_2 gas on the $MoTe_2$ surface (ESI, Fig. S2c and d,†). E_{2g}^1 and B_{2g}^1 intensities uniformly disappeared and remained after XeF_2 exposure. In particular, the E_{2g}^1 intensity remained and B_{2g}^1 mode completely disappeared in the 2 L region after XeF_2 exposure, implying that 2 L becomes uniform 1 L.

Scanning transmission electron microscopy (STEM) was used to identify the mysterious top layer of XeF_2-exposed $MoTe_2$. As shown in the cross-sectional STEM images of Fig. 2a, two $MoTe_2$ samples with different XeF_2 exposure times of 60 and 120 s at 1.8 torr showed a uniform and smooth layer of the same thickness (~2.5 nm) on top of intact $MoTe_2$. The underlying $MoTe_2$ might have remained intact, without any structural changes, even after XeF_2 exposure. The surface was continuously scanned using contact-mode AFM to evaluate the thickness of the oxidized layer. The topmost region of XeF_2-exposed $MoTe_2$ can be smoothly removed by using an AFM tip, as shown in Fig. 2b. The height profile based on the red dashed lines in Fig. 2b is shown in Fig. 2d. The exposed new surface had a difference in thickness of ~2.6 nm compared to the unexposed surface, which is consistent with the TEM results. The peeled area appeared as flat as the non-peeled area. In addition, the energy-dispersive X-ray spectroscopy (EDS) map in Fig. 2c clearly shows that the top region of XeF_2-exposed $MoTe_2$ contains more oxygen than the underlying region. Although it was challenging to quantitatively analyze the composition of the top region due to the resolution limit of the EDS and ultrathin sample, we could confirm that the top region of $MoTe_2$ was predominantly oxidized and disordered by XeF_2-exposure (a green dotted region indicates oxygen), while the lower $MoTe_2$ remained approximately intact even after XeF_2 exposure, showing only the Mo (purple dots) and Te (cyan-colored dots) spectra in EDS.

The AFM images in Fig. 3a show the surface morphology of XeF_2-exposed $MoTe_2$ for different times. The surface of XeF_2-exposed $MoTe_2$ is cleaner and smoother than plasma-treated $MoTe_2$ for a long exposure time of 270 s owing to the suppression of ion-bombardment effect.[31,32] The roughness and relative thickness of XeF_2-exposed $MoTe_2$ are plotted in Fig. 3b and c, respectively. The actual thicknesses of the flakes were measured using contact AFM. We did not observe a significant difference in the roughness of $MoTe_2$ even after a long exposure of 270 s (Fig. 3b). Thermodynamically, the XeF_2-treatment is possible to remove Mo or Te from the surface because the melting temperatures of MoF_6 and TeF_6 are lower than the room temperature.[33] Therefore, if a few top layers of $MoTe_2$ reacted with XeF_2, it would turn into a disordered structure with several broken bonds. Moreover, the disordered layer can be easily oxidized by exposing it to air after treating the surface with XeF_2 gas. Therefore, the broken structures can easily bond with oxygen when the sample is unloaded from the chamber. Some Mo–O bonds were expected to form at the surface defect sites, thinning the intrinsic $MoTe_2$.[34] In Fig. 3c, the relative thickness

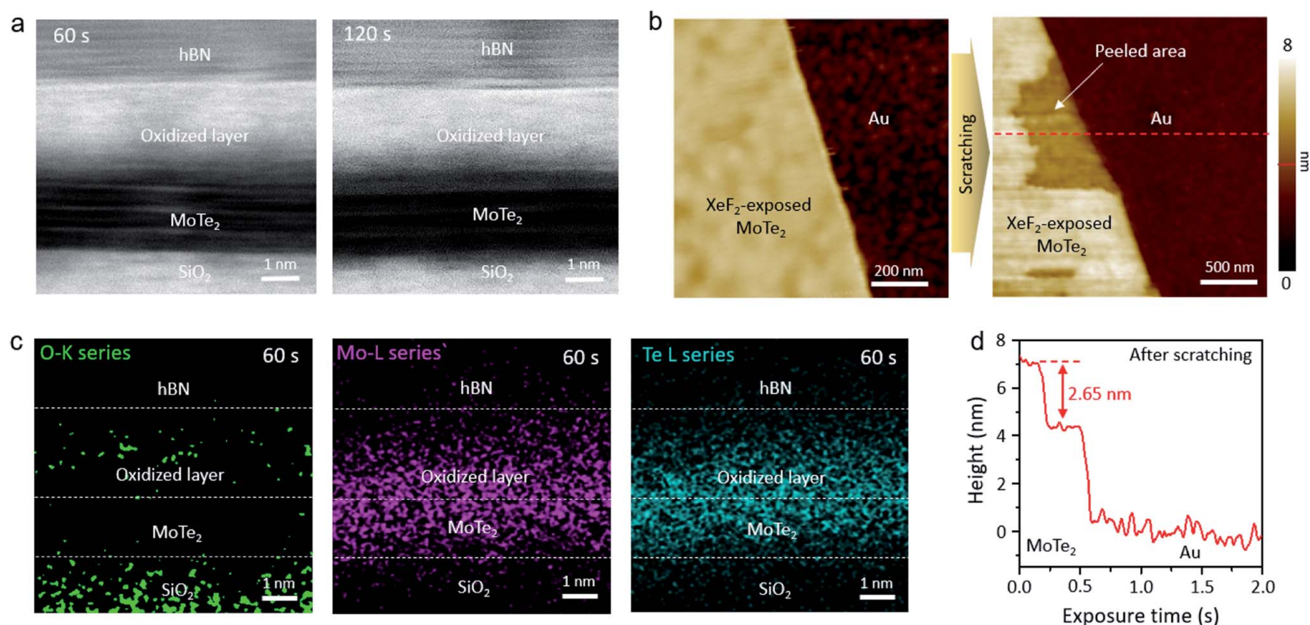

Fig. 2 (a) Cross-sectional STEM images of $MoTe_2$ after XeF_2 treatment at 1.8 torr for 60 s and 120 s, respectively, (b) AFM topology images of XeF_2 treated $MoTe_2$ before and after removing the surface layer by using a cantilever tip, (c) EDS mapping image of O-K, Mo-L and Te-L series of $MoTe_2$ after XeF_2 treatment at 1.8 torr for 60 s and (d) height profile of XeF_2 treated $MoTe_2$ after scratching by using a cantilever tip.

© 2022 The Author(s). Published by the Royal Society of Chemistry

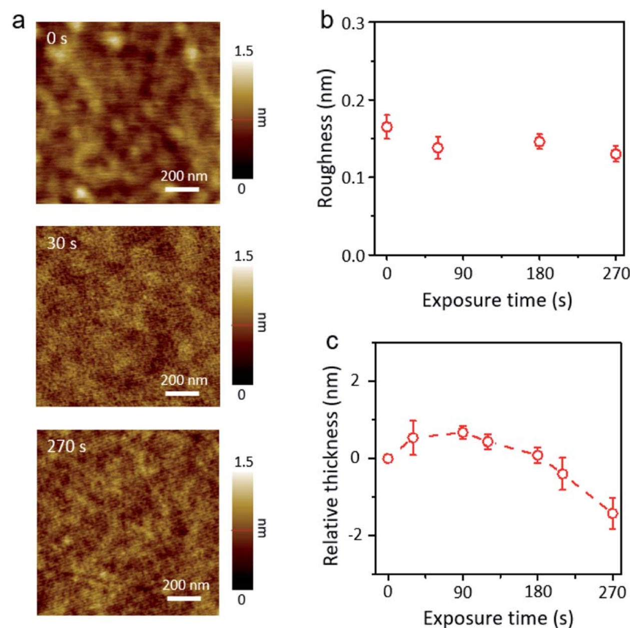

Fig. 3 (a) The AFM topology images of XeF_2 exposed $MoTe_2$ to show the uniform surface morphology after XeF_2 treatment for 0 s (as-exfoliated $MoTe_2$), 30 s and 270 s, respectively, (b) the root-mean-square (RMS) roughness of $MoTe_2$ after XeF_2 treatment at 1.8 torr with appropriate exposure times (from 0 s to 270 s) and (c) the relative height change of $MoTe_2$ as a function of increasing XeF_2 treatment time at 1.8 torr.

(the difference in thickness before and after XeF_2 exposure) was plotted as a function of the treatment time. The relative thickness of $MoTe_2$ gradually increased with the treatment time (from 0 to 120 s) after XeF_2 exposure because of the self-limiting growth mechanism of MoO_x.[35,36] This is consistent with the results illustrated in Fig. 2a (similar thicknesses of the oxidized layer after XeF_2 exposure for 60 and 120 s). However, the relative thickness decreased rather rapidly with the exposure time from 120 to 270 s. The formation of MoF_6 in the chamber can become more dominant than MoO_x due to the Gibbs free energies of MoF_6, MoO_2, and MoO_3 (*i.e.*, −1473.17, −533.0, and −668.1 J mol^{-1}, respectively).[33] Therefore, such a decrease in the thickness can be observed as MoF_6 can be easily removed owing to its low melting and boiling temperatures. When the available number of fluorine atoms decreased at a reduced pressure of 1 torr-60 s XeF_2 (ESI, Fig. S3a and b,†), the number of bonding between carbon (C) and fluorine (F) atom should be limited, which revealed the nanohole surface on the $MoTe_2$ surface. In this case, while the relative thickness was just negligibly changed (ESI, Fig. S3d†), the surface roughness became deteriorated, as shown in ESI, Fig. S3c.† We used the same conditions—fabrication of a uniform oxidized layer with no nanoholes on $MoTe_2$ with XeF_2 gas of 1.8 torr—for other experiments. Changes in the morphology due to various treatments in 2D materials devices often lead to reduced electrical contact.[37–39] We directly fabricated smooth and uniform oxidized layers on $MoTe_2$ through XeF_2 gas under the conditions of 1.8 torr within 120 s. The XeF_2 exposure method is easier to scale-up compared with previous methods, such as laser, plasma and thermal annealing.[40–42]

Photoelectron spectroscopy (PES) with a photon energy of 780 eV was performed under ultra-high vacuum conditions to identify the top layer of $MoTe_2$ before (black dotted lines) and after (red dotted lines) exposure to XeF_2 (Fig. 4a–d). In each figure, the top-(bottom-) panel shows the core-level spectrum before (after) the treatment. We note that the $MoTe_2$ flakes were treated with XeF_2 gas at 1.8 torr for 60 s for PES-characterization. The Mo 3d core level from $MoTe_2$ showed the binding energies of Mo $3d_{5/2}$ at 228.4 eV and Mo $3d_{3/2}$ at 231.9 eV before XeF_2 exposure, agreeing with the previous report (Fig. 4a).[43] This indicates that the as-prepared $MoTe_2$ sample has high crystallinity. However, mixed states of Mo^{4+} and Mo^{6+} were observed after XeF_2 exposure of 60 s (red dotted lines), supporting the partial oxidation of molybdenum. Additionally, the Te–O bonds in the XPS spectra showed two peaks at 576.3 eV and 587.1 eV (upper graph of Fig. 4b, red dotted lines). The more interesting result is that the Mo 3d and Te 3d peaks are downshifted to almost the same extent (∼0.7 eV). The peak downshifts can be assigned to hole-doping, since the Fermi level, which represents zero energy, moves further away from the conduction band with hole-doping.[44,45] Besides, the previously suggested Raman spectra also support that the p-type doping occurred after XeF_2 exposure (ESI, Fig. S2b†). As expected, the O 1s core level appeared after XeF_2 exposure (Fig. 4c). No peak related to H_2O (∼532 eV [30]) was found because PES was performed under ultra-high vacuum conditions immediately after mechanically exfoliating $MoTe_2$. The O 1s core-level spectrum together with the occurrence of Mo^{6+} in Mo 3d strongly indicates that an oxidized layer was formed, such as MoO_x.[46] Lastly, the F 1s peak (Fig. 4d) shows that a small number of fluorine atoms are chemically bonded. Hence, MoO_x, a disordered oxide layer containing negligible fluorine atoms, was formed, playing an important role in doping.

The valence band edges of the samples were investigated using PES ($h\nu$ = 90 eV), as shown in Fig. 4e. The valence band edge of $MoTe_2$ before (black) and after (red) XeF_2 exposure was found to be positioned at ∼0.8 eV and ∼3.0 eV below the Fermi level, respectively. The valence band edge of XeF_2-treated $MoTe_2$ shifted to about 3.0 eV, which is close to the value of the MoO_x phase.[47] Interestingly, MoO_x does not contain a high density of defects (gap states) inside both $MoTe_2$ surfaces before (black) and after (red) XeF_2 exposure. The ultrathin oxidized layer can completely change the band diagram. Also, the secondary electron cutoffs (Fig. 4f) show that the work functions of the samples were positioned at ∼4.8 (pristine $MoTe_2$) and ∼5.6 eV (MoO_x), respectively, due to the formation of a non-stoichiometric oxidation phase after XeF_2 exposure. The work function of XeF_2-exposed $MoTe_2$ was smaller than that (∼6.8 eV) of MoO_3.[48] Therefore, the result indicates that only a few topmost surface layers of $MoTe_2$ (3 L in Fig. 1) were substituted with MoO_x with a comparable atomic thickness, while the subsurface (1 L in Fig. 1) still remained as $MoTe_2$; however, the overall thickness was scarcely changed by XeF_2-treatment within a limited exposure time. A schematic image of $MoTe_2$ before and after XeF_2 exposure is shown in ESI, Fig. S4.† The 4 L of $MoTe_2$ was

 © 2022 The Author(s). Published by the Royal Society of Chemistry

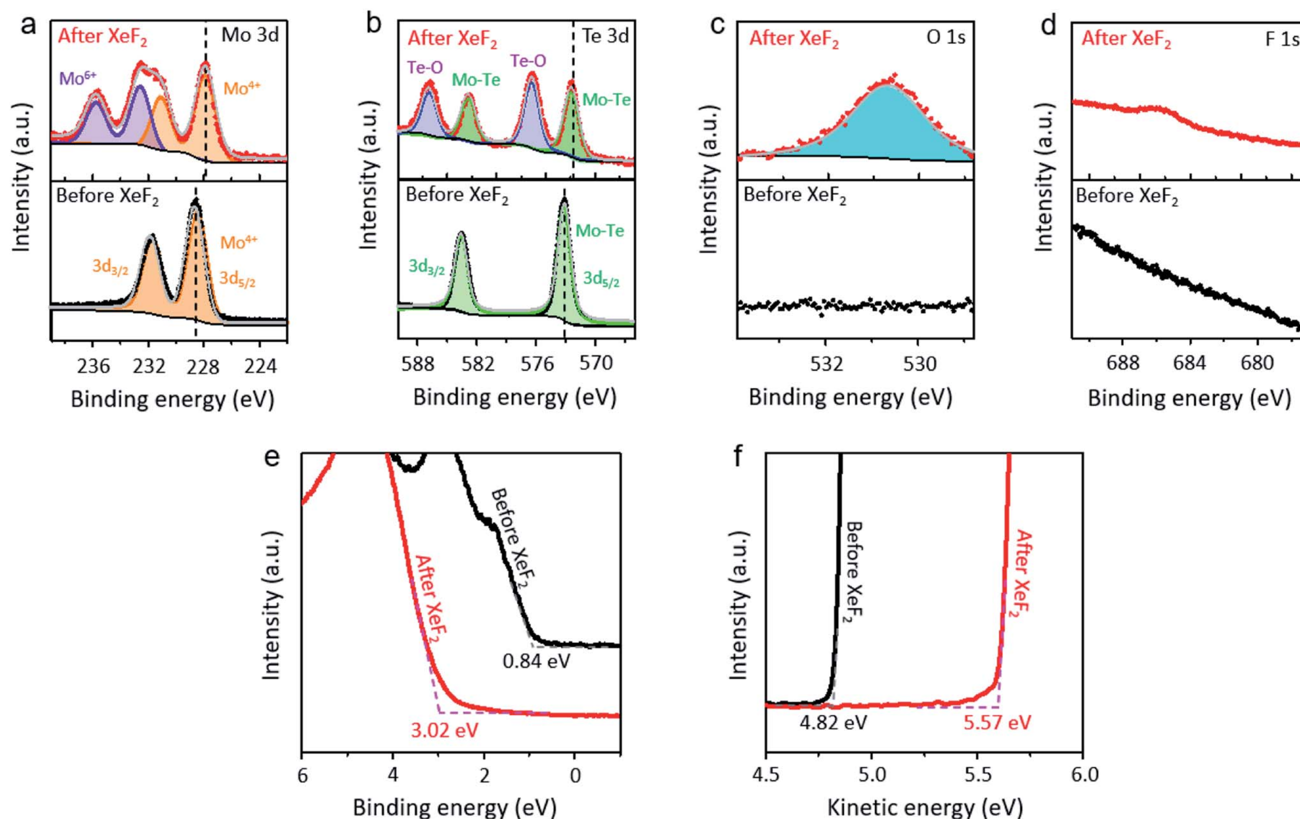

Fig. 4 (a–d) PES spectra with a photon energy of 780 eV of 2H-$MoTe_2$ without and with XeF_2 treatment at 1.8 torr for 60 s; the bottom spectra of PES show $MoTe_2$ before XeF_2 treatment and the top spectra of PES show that after XeF_2 treatment at 1.8 torr for 60 s. (a) Mo 3d spectra, (b) Te 3d spectra, (c) O 1s spectra and (d) F 1s spectra. (e and f) PES ($h\nu = 90$ eV) of 2H-$MoTe_2$ without and with XeF_2 treatment at 1.8 torr for 60 s; the black lines show the spectra of PES before XeF_2 treatment and the red lines show the spectra of PES after XeF_2 treatment at 1.8 torr for 60 s. (e) The valence edge of $MoTe_2$ before and after XeF_2 exposure and (f) the secondary electron cutoffs of $MoTe_2$ before and after XeF_2 exposure.

converted to a 1 L of $MoTe_2$ with an oxidized layer at 1.8 torr for 150 s. The 3 L of the $MoTe_2$ crystal structure disappeared after XeF_2 exposure, forming the remaining oxidized layer.

We fabricated $MoTe_2$ FETs by forming contacts in the XeF_2-exposed regions because the ultrathin oxidized layer of XeF_2-exposed $MoTe_2$ can be used as a buffer layer between $MoTe_2$ and the metal. Multilayer $MoTe_2$ with a thickness of ~3 nm was used for device fabrication. Two different types of contacts were fabricated on the same $MoTe_2$ flakes (ESI, Fig. S5† shows the detailed device fabrication process). Electrodes were patterned by e-beam lithography and exposed to XeF_2 for 60 s, followed by e-beam deposition of metals (Cr 1 nm/Pd 30 nm/Au 40 nm) to fabricate the contacts in the XeF_2-exposed regions. Cr is an adhesion layer; Pd can be connected to $MoTe_2$ for p-type FETs. Metals were also deposited on the surface of the pristine $MoTe_2$ for comparison. As shown in Fig. 5a, the $MoTe_2$ FET with conventional metal contacts showed a low field-effect hole mobility of 0.07 $cm^2\ V^{-1}\ s^{-1}$ with an on/off current ratio of $\sim 10^4$, probably because of the high contact resistance (see the non-linear output curves (I_{ds}–V_{ds}) in the inset). Furthermore, the $MoTe_2$ FET with XeF_2-exposed contacts exhibited two orders of magnitude higher hole mobility (6.31 $cm^2\ V^{-1}\ s^{-1}$) with a higher on/off current ratio of $\sim 10^5$. Particularly, the linear output curves in the inset of Fig. 5b show the ohmic nature of XeF_2-exposed contacts. The linear-scale transfer curves of the two devices in Fig. 5c clearly show that the on-current of the $MoTe_2$ FET with XeF_2-exposed contacts is significantly higher than that of the $MoTe_2$ FET with conventional metal contacts. The type and height of the Schottky barrier formed at the contact between the metal and the TMDs can determine the contact resistivity. However, the metal-insulator-semiconductor structure with an ultrathin insulating layer can substantially relieve the Fermi level pinning effect by reducing the direct metal contact to the interfacial states of $MoTe_2$.[49] The XeF_2-vapor process can chemically react with only a few topmost layers of TMDs, minimizing the degradation of underlying $MoTe_2$ crystallinity.[34] In addition, the oxidized layer induces p-doping of the underlying $MoTe_2$. Therefore, the ultrathin oxide interlayer enables overcoming the Schottky barrier induced by Fermi level pinning at the semiconductor–metal junction, reducing the contact resistance in the $MoTe_2$ devices (see the band diagram in Fig. 5d). The uniform oxide interlayer only with several nm-thickness can be easily and precisely produced through our method. In particular, the oxygen plasma treatment method was suitable for scale up, but uniform surface cannot be achieved due to ion bombardment on the $MoTe_2$ surface.[35] Laser treatment is also widely used to improve the properties of contact between the metal and $MoTe_2$,[50] but there

© 2022 The Author(s). Published by the Royal Society of Chemistry

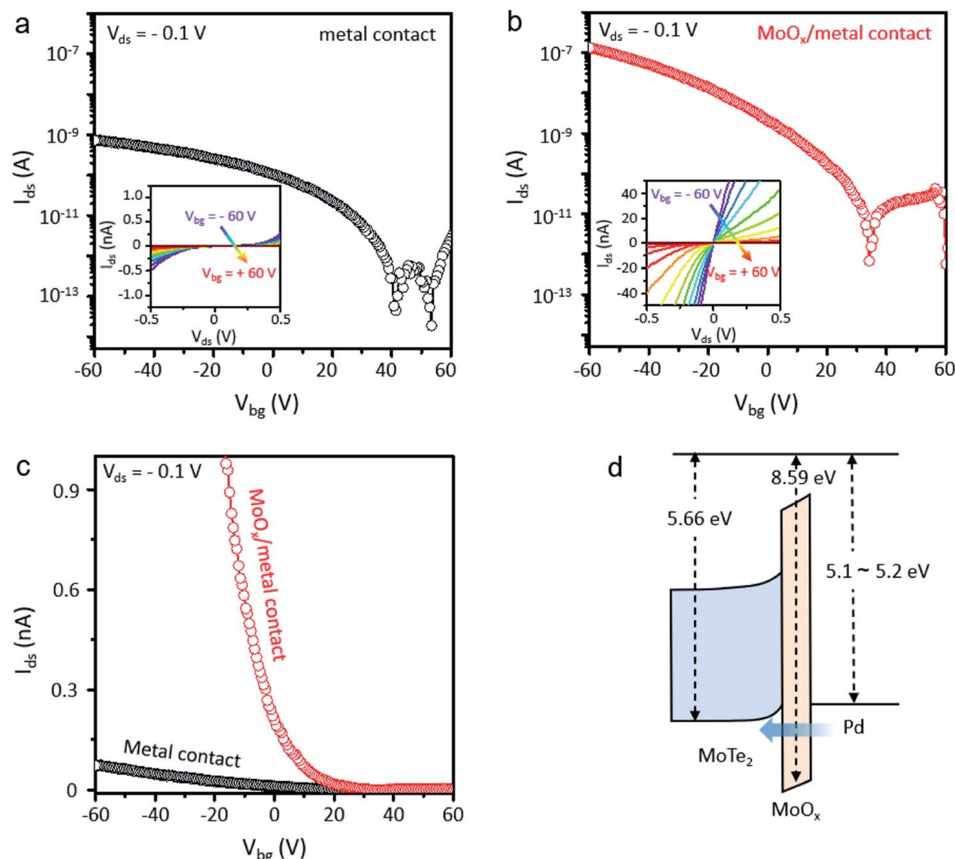

Fig. 5 (a) $I_{ds}-V_g$ transfer characteristics of $MoTe_2$ FETs with and without the XeF_2 treatment process in the logarithmic scale. The black dotted line curve shows the transfer characteristics of the $MoTe_2$ channel with direct contact between the metal and $MoTe_2$. (b) The red dotted line curve shows the transfer characteristics of the $MoTe_2$ channel with contact between the metal and $MoO_x/MoTe_2$ in the logarithmic scale. The insets of Fig. 5a and b show $I_{ds}-V_{ds}$ output characteristics of the $MoTe_2$ FET without XeF_2 treatment in the contact region (Fig. 5a) and with XeF_2 treatment in the contact region (Fig. 5b) before metal deposition. (c) $I_{ds}-V_g$ transfer characteristics of $MoTe_2$ FETs both conventional metal contacts (black dots) and MoO_x/metal contacts (red dots) in the linear scale and (d) the schematic image of the band diagram for $MoTe_2$,[15] oxidized layer, and Pd.[21,51,52]

is a limitation to scale up. Therefore, our XeF_2-mediated oxidation technique is a promising candidate for fabricating high-performance electronic devices based on $MoTe_2$.

Conclusions

In conclusion, we demonstrate a controllable technique to produce a uniform oxidized layer on top of $MoTe_2$ by XeF_2 exposure. XeF_2-exposed $MoTe_2$ was formed with a thin and uniform oxidized layer ($\sim$2.5 nm-thick MoO_x) regardless of the exposure time (within $\sim$120 s) because of the passivation effect and simultaneous etching. We could directly fabricate the ultra-smooth thin oxidized layer on $MoTe_2$ by the simple and easy XeF_2 vapor exposure method. In addition, the electrical properties of $MoTe_2$ FETs with and without XeF_2 treatment in the contact region were measured, including the hole mobility and on/off current ratio. The $MoTe_2$ FET with an ultra-smooth MoO_x interlayer shows a relatively high field-effect hole mobility of 6.31 $cm^2\ V^{-1}\ s^{-1}$ with a high on/off current ratio of $\sim 10^5$. This result is two orders of magnitude higher than that of $MoTe_2$ FETs with conventional metal contacts (0.07 $cm^2\ V^{-1}\ s^{-1}$). The simplicity and applicability of our method will be useful for practical applications of $MoTe_2$ FETs in the future.

Experimental section

Sample preparation

$MoTe_2$ was mechanically exfoliated onto the SiO_2 (280 nm)/Si substrate after the substrate was cleaned with acetone and isopropyl alcohol (IPA) in an ultra-sonication bath for 10 min, respectively. The exfoliated $MoTe_2$ flakes were loaded into a XeF_2 chamber (ESI, Fig. S1†). The XeF_2 gas of high pressure (1.8 torr) was introduced into the chamber in a cyclic manner, where the chamber was filled with XeF_2 for different treatment times in a cycle and then pumped out.

Raman spectroscopy

The optical properties of $MoTe_2$ were observed through Raman spectroscopy (Renishaw, inVia), with a laser wavelength of 532 nm and a spot size of $\sim$1 μm. Raman spectra at the same position on $MoTe_2$ were obtained before and after XeF_2 exposure.

© 2022 The Author(s). Published by the Royal Society of Chemistry

Atomic force microscopy (AFM)

Atomic force microscopy (AFM, Park systems, NX10) was used to observe the surface morphology, roughness, and thickness of the $MoTe_2$ samples. The contact mode was used for exact thickness information. A silicon tip with an elastic constant of $\sim$0.2 N m^{-1} was used in contact mode.

Transmission electron microscopy (TEM)

For cross-sectional TEM, a focused ion beam (FIB) system (Helios G4, Thermo Fisher Scientific, USA) was used. To protect the sample surface from e-beam, the XeF_2-exposed $MoTe_2$ flakes were covered with multilayer h-BN. We used TEM (JEM-F200, JEOL Ltd, Japan) with a low operating voltage of 80 keV. Transmission electron microscopy-energy dispersive X-ray spectroscopy (TEM-EDS) was used to analyze the atomic ratios.

Photoemission spectroscopy (PES)

$MoTe_2$ crystals were prepared on an Au-coated SiO_2 substrate. Photoelectron spectroscopy (PES) spectra of the sample were recorded at $h\nu = 780$ eV. In addition, valence spectra and secondary electron cutoff were measured using a photon energy of $h\nu = 90$ eV. Synchrotron-based PES spectroscopy was performed at room temperature at the 4D beamline in the Pohang Light Source II (PLS II), Korea.

Device fabrication and electrical measurements

$MoTe_2$ field-effect transistors (FETs) were fabricated on a SiO_2 (285 nm)/Si substrate using e-beam lithography (EBL, TESCAN). Metal contacts were deposited by using an e-beam evaporator (Temescal six pocket e-beam evaporation systems). The $MoTe_2$ FETs were measured by using a semiconductor parameter analyzer (Keithley 4200). The source-drain current (I_{ds}) was measured with a fixed source-drain voltage (V_{ds}) of -0.1 V and varying back-gate voltage (V_{bg}) from -60 V to 60 V. The field-effect mobility (μ_{FE}) was calculated, extracting from the linear area of the transfer curve. The equation is $\mu_{FE} = [(\Delta I_{ds}/\Delta V_{bg})(L/W)V_{ds}]/C_{ox}$, where Δ, W, L, and C_{ox} are the gradient of I_{ds} to V_{ds}, channel width, length and gate capacitance of SiO_2 (12.1 nF cm^{-2} for a SiO_2 thickness of 285 nm).

Author contributions

E. J. and J. H. K. contributed equally. E. J., J. H. K., and G. -H. L. designed this work. E. J. and J. H. K. performed all experiments including AFM, Raman spectroscopy, PES, and STEM analysis. W. L. performed the Xenon difluoride (XeF_2) experiments. K. I performed the photoemission spectroscopy (PES) system. E. J. and J.-C. S fabricated the device and analyzed device performance. All authors discussed the results. E. J. and J. H. K. wrote the manuscript together. J.-W. P, H. S and G.-H. L reviewed and edited the manuscript together. All authors have given approval to the final version of the manuscript.

Conflicts of interest

The authors declare no competing financial interest.

Acknowledgements

This research was supported by the Basic Science Research Program through the National Research Foundation of Korea (NRF) funded by the Ministry of Science, ICT & Future Planning (2021R1A2C3014316) and the National Research Foundation of Korea (NRF) funded by the Ministry of Science and ICT (2021M3F3A2A01037858). Experiments at PLS-II were supported by MSIP-R. O., Korea. This paper was also a result of the research project supported by SK Hynix Inc.

References

1 B. Radisavljevic, A. Radenovic, J. Brivio, V. Giacometti and A. Kis, *Nat. Nanotechnol.*, 2011, **6**, 147–150.
2 Z. Yin, H. Li, H. Li, L. Jiang, Y. Shi, Y. Sun, G. Lu, Q. Zhang, X. Chen and H. Zhang, *ACS Nano*, 2012, **6**, 74–80.
3 S. Fathipour, N. Ma, W. Hwang, V. Protasenko, S. Vishwanath, H. Xing, H. Xu, D. Jena, J. Appenzeller and A. Seabaugh, *Appl. Phys. Lett.*, 2014, **105**, 192101.
4 J. Y. Lim, M. Kim, Y. Jeong, K. R. Ko, S. Yu, H. G. Shin, J. Y. Moon, Y. J. Choi, Y. Yi and T. Kim, *npj 2D Mater. Appl.*, 2018, **2**, 1–7.
5 N. Huo, S. Tongay, W. Guo, R. Li, C. Fan, F. Lu, J. Yang, B. Li, Y. Li and Z. Wei, *Adv. Electron. Mater.*, 2015, **1**, 1400066.
6 S. Yu, J. S. Kim, P. J. Jeon, J. Ahn, J. C. Park and S. Im, *Adv. Funct. Mater.*, 2017, **27**, 1603682.
7 H. S. Lee, S. W. Min, M. K. Park, Y. T. Lee, P. J. Jeon, J. H. Kim, S. Ryu and S. Im, *Small*, 2012, **8**, 3111–3115.
8 H. Y. Chang, M. N. Yogeesh, R. Ghosh, A. Rai, A. Sanne, S. Yang, N. Lu, S. K. Banerjee and D. Akinwande, *Adv. Mater.*, 2016, **28**, 1818–1823.
9 N. Haratipour and S. J. Koester, Multi-layer MoTe2 p-channel MOSFETs with high drive current, in, *72nd Device Research Conference*, IEEE, 2014, pp. 171–172.
10 M. Grzeszczyk, K. Gołasa, M. Zinkiewicz, K. Nogajewski, M. R. Molas, M. Potemski, A. Wysmołek and A. Babiński, *2D Materials*, 2016, **3**, 025010.
11 N. R. Pradhan, D. Rhodes, S. Feng, Y. Xin, S. Memaran, B.-H. Moon, H. Terrones, M. Terrones and L. Balicas, *ACS Nano*, 2014, **8**, 5911–5920.
12 A. V. Penumatcha, R. B. Salazar and J. Appenzeller, *Nat. Commun.*, 2015, **6**, 1–9.
13 Y. F. Lin, Y. Xu, C. Y. Lin, Y. W. Suen, M. Yamamoto, S. Nakaharai, K. Ueno and K. Tsukagoshi, *Adv. Mater.*, 2015, **27**, 6612–6619.
14 C. M. Smyth, R. Addou, C. L. Hinkle and R. M. Wallace, *J. Phys. Chem. C*, 2020, **124**, 14550–14563.
15 C. Kim, I. Moon, D. Lee, M. S. Choi, F. Ahmed, S. Nam, Y. Cho, H.-J. Shin, S. Park and W. J. Yoo, *ACS Nano*, 2017, **11**, 1588–1596.

© 2022 The Author(s). Published by the Royal Society of Chemistry

16 S. McDonnell, A. Azcatl, R. Addou, C. Gong, C. Battaglia, S. Chuang, K. Cho, A. Javey and R. M. Wallace, *ACS Nano*, 2014, **8**, 6265–6272.
17 R.-S. Chen, G.-L. Ding, Y. Zhou and S.-T. Han, *J. Mater. Chem. C*, 2021, **9**, 11407–11427.
18 X. Liu, C. Wang, S. Yi and Y. Gao, *Org. Electron.*, 2014, **15**, 977–983.
19 S. Lee, A. Tang, S. Aloni and H.-S. Philip Wong, *Nano Lett.*, 2016, **16**, 276–281.
20 Y.-H. Chen, C.-Y. Cheng, S.-Y. Chen, J. S. D. Rodriguez, H.-T. Liao, K. Watanabe, T. Taniguchi, C.-W. Chen, R. Sankar and F.-C. Chou, *npj 2D Mater. Appl.*, 2019, **3**, 1–7.
21 S. Chuang, C. Battaglia, A. Azcatl, S. McDonnell, J. S. Kang, X. Yin, M. Tosun, R. Kapadia, H. Fang and R. M. Wallace, *Nano Lett.*, 2014, **14**, 1337–1342.
22 Y. Liu, H. Nan, X. Wu, W. Pan, W. Wang, J. Bai, W. Zhao, L. Sun, X. Wang and Z. Ni, *ACS Nano*, 2013, **7**, 4202–4209.
23 H. Zhang, Y. Wan, Y. Ma, W. Wang, Y. Wang and L. Dai, *Appl. Phys. Lett.*, 2015, **107**, 101904.
24 P. Blake, E. Hill, A. Castro Neto, K. Novoselov, D. Jiang, R. Yang, T. Booth and A. Geim, *Appl. Phys. Lett.*, 2007, **91**, 063124.
25 T. Wieting, A. Grisel and F. Levy, *Phys. B+C*, 1980, **99**, 337–342.
26 M. Yamamoto, S. T. Wang, M. Ni, Y.-F. Lin, S.-L. Li, S. Aikawa, W.-B. Jian, K. Ueno, K. Wakabayashi and K. Tsukagoshi, *ACS Nano*, 2014, **8**, 3895–3903.
27 B. Zheng, Z. Wang, Y. Chen, W. Zhang and X. Li, *2D Materials*, 2018, **5**, 045011.
28 Y. Zhang, H. Wu, Z. Liu, S. Xie and J. Li, *Journal of Materiomics*, 2021, **7**, 347–354.
29 L. Kumari, Y.-R. Ma, C.-C. Tsai, Y.-W. Lin, S. Y. Wu, K.-W. Cheng and Y. Liou, *Nanotechnology*, 2007, **18**, 115717.
30 X. Zheng, Y. Wei, C. Deng, H. Huang, Y. Yu, G. Wang, G. Peng, Z. Zhu, Y. Zhang and T. Jiang, *ACS Appl. Mater. Interfaces*, 2018, **10**, 30045–30050.
31 H. Nan, R. Zhou, X. Gu, S. Xiao and K. K. Ostrikov, *Nanoscale*, 2019, **11**, 19202–19213.
32 J. Shim, A. Oh, D. H. Kang, S. Oh, S. K. Jang, J. Jeon, M. H. Jeon, M. Kim, C. Choi and J. Lee, *Adv. Mater.*, 2016, **28**, 6985–6992.
33 J. G. Speight, *Lange's Handbook of Chemistry*, McGraw-Hill Education, 2017.
34 R. Zhang, D. Drysdale, V. Koutsos and R. Cheung, *Adv. Funct. Mater.*, 2017, **27**, 1702455.
35 Q. Wang, J. Chen, Y. Zhang, L. Hu, R. Liu, C. Cong and Z.-J. Qiu, *Nanomaterials*, 2019, **9**, 756.
36 M. Yamamoto, S. Dutta, S. Aikawa, S. Nakaharai, K. Wakabayashi, M. S. Fuhrer, K. Ueno and K. Tsukagoshi, *Nano Lett.*, 2015, **15**, 2067–2073.
37 J. Jang, Y. Kim, S.-S. Chee, H. Kim, D. Whang, G.-H. Kim and S. J. Yun, *ACS Appl. Mater. Interfaces*, 2019, **12**, 5031–5039.
38 C. M. Smyth, R. Addou, C. L. Hinkle and R. M. Wallace, *J. Phys. Chem. C*, 2019, **123**, 23919–23930.
39 M. Li, F. Lan, W. Yang, Z. Ji, Y. Zhang, N. Xi, X. Xin, X. Jin and G. Li, *Nanotechnology*, 2020, **31**, 395713.
40 A. Castellanos-Gomez, M. Barkelid, A. Goossens, V. E. Calado, H. S. van der Zant and G. A. Steele, *Nano Lett.*, 2012, **12**, 3187–3192.
41 J. Wu, H. Li, Z. Yin, H. Li, J. Liu, X. Cao, Q. Zhang and H. Zhang, *Small*, 2013, **9**, 3314–3319.
42 X. Lu, M. I. B. Utama, J. Zhang, Y. Zhao and Q. Xiong, *Nanoscale*, 2013, **5**, 8904–8908.
43 D. Qu, X. Liu, M. Huang, C. Lee, F. Ahmed, H. Kim, R. S. Ruoff, J. Hone and W. J. Yoo, *Adv. Mater.*, 2017, **29**, 1606433.
44 A. Nipane, D. Karmakar, N. Kaushik, S. Karande and S. Lodha, *ACS Nano*, 2016, **10**, 2128–2137.
45 J. H. Kim, J. Lee, J. H. Kim, C. Hwang, C. Lee and J. Y. Park, *Appl. Phys. Lett.*, 2015, **106**, 251606.
46 J. Chastain and R. C. King Jr, *Perkin-Elmer, Handbook of X-ray Photoelectron Spectroscopy*, Perkin-Elmer, USA, 1992, p. 261.
47 X. Zheng, X. Zhang, Y. Wei, J. Liu, H. Yang, X. Zhang, S. Wang, H. Xie, C. Deng and Y. Gao, *Nano Res.*, 2020, **13**, 952–958.
48 J. Meyer, S. Hamwi, M. Kröger, W. Kowalsky, T. Riedl and A. Kahn, *Adv. Mater.*, 2012, **24**, 5408–5427.
49 M. Farmanbar and G. Brocks, *Phys. Rev. B*, 2016, **93**, 085304.
50 S.-Y. Seo, J. Park, J. Park, K. Song, S. Cha, S. Sim, S.-Y. Choi, H. W. Yeom, H. Choi and M.-H. Jo, *Nat. Electron.*, 2018, **1**, 512–517.
51 M. Fontana, T. Deppe, A. K. Boyd, M. Rinzan, A. Y. Liu, M. Paranjape and P. Barbara, *Sci. Rep.*, 2013, **3**, 1–6.
52 W.-M. Kang, S. Lee, I.-T. Cho, T. H. Park, H. Shin, C. S. Hwang, C. Lee, B.-G. Park and J.-H. Lee, *Solid-State Electron.*, 2018, **140**, 2–7.

© 2022 The Author(s). Published by the Royal Society of Chemistry